Effects of the geometrical configuration of air-water mixer on the size and distribution of micro-bubbles in aeration systems

Alessio Basso[a] , Faik Hamad[a,*] and Poobalan Ganesan[b]

[a]*School of Science Engineering and Design, Teesside University, Middlesbrough, Tees Valley, TS1 3BX, UK*
[b]*Department of Mechanical Engineering, University of Malaya, Kuala Lumpur, Malaysia*

Abstract

The objective of this work is to present a novel geometrical configuration for micro-bubble generators (MBGs) to improve dissolved-oxygen levels in water. Among various methodologies from the literature, Orifice and Venturi tubes have been considered as baseline cases. Experimental data from the literature are used to verify a CFD case developed for a better understanding of the dynamics of microbubble generators. As a result, the validated CFD setup has been implemented on a modified Venturi-type generator, where air is injected coaxially with respect to the tube axis, while a helicoid wall at variable pitch angle is used. Results show a reduction in the mean bubble diameter distribution from the baseline Venturi tubes, particularly, at low-speed inlet velocities. This is of interest, especially to decrease the energy requirement for most common water aeration systems.

Keywords: microbubble generator, dissolved oxygen in water, swirling flow, CFD simulation

* *Correspondence author.*
E-mail address: f.hamad@tees.ac.uk

1. Introduction

Air microbubbles in water are essential to manipulate levels of dissolved oxygen, [1] which in aquaculture facilities – e.g. shrimp farms – can help to control growth rate and amount of waste waters produced. [2, 3] In fact, depending on the mean diameter, bubble clouds can release various amounts of oxygen in water through shrinking, before collapse. Bubble distributions are classified as follows:

- Macrobubbles, defined by a diameter D > 100 μm. With such great diameter, buoyancy force is crucial for bubbles to determine the rising speed in vertical water columns towards the water surface, where eventually bursting occurs. Some studies [4, 5] have demonstrated that bubbles with diameter equal to 1 mm can move at a rate of 5 to 6 m/min.
- Microbubbles are known for their diameter being in the range 10 μm < D < 50 μm. As a result, they can persist in water for longer time compared to macrobubbles. Endo et al. [6] have estimated that microbubbles with diameter equal to 10 μm can rise at 3 mm/min.
- Nanobubbles, with diameter D < 0.2 μm, can persist in water for weeks or months before dissolution. [7, 5] Their long life is due to strong hydrogen bonds, similar to ice molecules. Takahashi et al. [7] have calculated that nanobubbles with diameter of 3.5 nm or smaller can indefinitely persist in water. In this condition - where viscous drag, buoyancy and bubble weight are in static equilibrium.

Following the definitions above, we believe that both macrobubbles and nanobubbles are not suitable for water test facilities. In fact, the former cannot release sufficient dissolved oxygen, due to the high rising speed; the latter take extensive time period to shrink. Therefore, our aim in this work is to produce uniform microbubble distributions with mean diameter below 50 μm. [8, 9] Our assumption is based on similar distributions which are already effective in dissolved air flotation (DAF), [10, 11] waste-water treatment, [12, 13, 14, 15] mining processes [16, 17] and crude-oil refinement [18].

A number of different configurations of microbubble generators have been developed over the past few years. Sadatomi et al. [8] have proposed a system characterized by an inner spherical model, inducing air suction through a porous wall, due to the low-pressure region behind the sphere. In a further development, [19] an inner coaxial orifice has replaced the spherical body. Thus far, Sadatomi's MBGs have produced distributions where 70% of microbubbles have diameter of the order of 100μm. Other methods make use of swirling flows [20] and stirring through rotating porous plates [9] to produce distributions with mean values equal to 20 μm and 50

μm respectively. However, all the above systems require an additional energy input to move rotating components. By contrast, Venturi generators have a simple design and require less power. In fact, similarly to orifice-type tubes, pressure recovery (downstream of the throat section) and turbulent mixing are the main physical mechanisms affecting the final distribution of microbubbles at the tube outlet. Kawamura et al [21] suggested that coalescence of microbubbles is due to the axial flow acceleration at the throat section, whereas pressure recovery in the diffuser can induce sharp shear stresses responsible for bubble breakup. At the same time, Kawashima et al [22] attributed the bubbles breakup in the diffuser to supersonic flow for the air-water mixture. By implementing the same principle, Ishikawa et al. [23] and Gordiychuk et al. [24] were able to generate microbubbles with mean diameter of 50μm through Venturi-type generators.

The size of bubbles in two-phase gas-liquid mixtures can be controlled either a) in the injection process (inlet velocity and injector diameter) of the dispersed phase or b) in flow parameters, such as mixture velocity and volumetric quality. At present, we are interested in the cloud mean diameter to estimate how efficient our microbubble generator is. In a future experimental validation of this work, we will be able to assess the system efficiency based on the energy input required to aerate a finite volume of water and the net oxygen mass transfer in water.

Therefore, three are the objectives of this work. Firstly, we intend to review the existing MBG technology to identify the best design, based on performance and microbubble distributions produced. Secondly, we aim at validating our CFD setup to predict the bubble distribution, by comparison with experimental data from literature. Thirdly, we propose a novel configuration which is investigated and compared through CFD with its respective baseline design, and which will be manufactured and tested in the laboratory.

2. Microbubble generators

2.1 Orifice-type tubes

One configuration explored in this research is the orifice-type tube which was first designed and investigated by Sadatomi et al. [19] (Figure 1). Water is introduced longitudinally through an axial orifice, while air is sucked from a porous annular wall, due to the pressure drop downstream of the orifice.

(a)

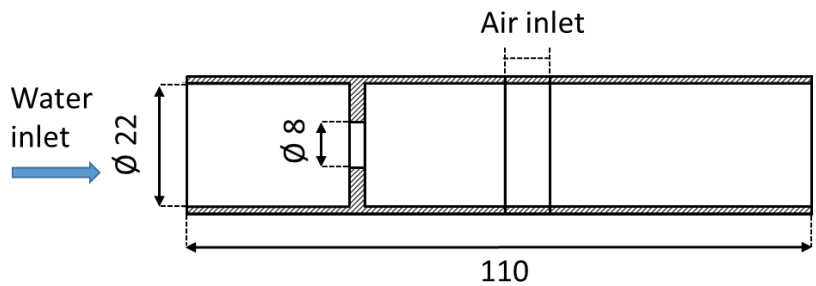

(b)

Figure 1. Orifice-type MBG analysed in this work: a) 3D view, b) longitudinal section schematic. Dimensions are in mm.

Water inlet flow and air injection rates have been tuned for three different orifice diameters (Table 1). The porous wall is composed of punched holes of mean diameter $d_H = 300$ µm, which extend over a longitudinal length $h_H = 8$ mm.

Table 1. Orifice microbubble generator, test cases.

Orifice diam. d_o [mm]	Air flow Q_g [l/min]	Vol. quality α [%]
8.8	1.0 4.0 1.0 4.0	2.22 8.33 1.88 7.14
12.5	1.0 4.0 1.0 4.0	1.72 6.56 1.49 5.71
14.6	1.0 4.0 1.0 4.0	1.49 5.71 1.37 5.26

2.2 Venturi-type tubes

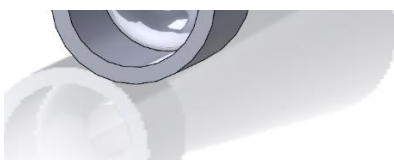

(a)

igated by Kawashima et al. [22] and ich for brevity we name as baseline - divergent duct where water and air ong the tube axis (

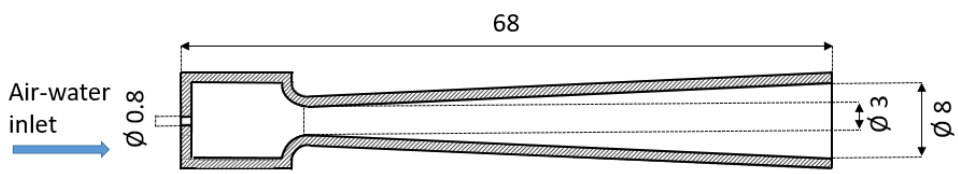

(b)

Figure 2). Test cases are detailed in Table 2, where the volumetric quality is defined as the ratio between the air inlet flow rate and the mixture flow rate, namely $\alpha = Q_G/(Q_G + Q_L)$. Furthermore, the velocity in the centre line of the throat section of the tube is used to calculate the inlet flow rate of water, based on the Bernoulli's equation for incompressible flows.

(a)

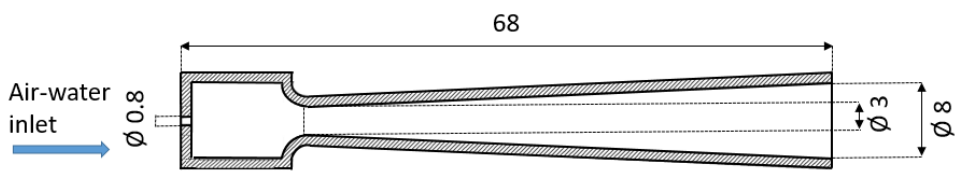

(b)

Figure 2. Venturi baseline MBG: a) 3D sketch and b) section. Dimensions are in mm.

Table 2. Venturi baseline microbubble generator. Test cases.

Throat velocity u_{th} [m/s]	Air flow Q_G[l/min]	Vol. quality α [%]

9.4 16.0 21.2 25.9	1.0 4.0 1.0 4.0	4.0 4.0 4.0 4.0
9.4 16.0 21.2 25.9	1.0 4.0 1.0 4.0	8.0 8.0 8.0 8.0
9.4 16.0 21.2 25.9	1.0 4.0 1.0 4.0	20.0 20.0 20.0 20.0

3. CFD model and simulation

3.1 Continuous Phase

Numerical simulations have been carried out using ANSYS Fluent 18.1. The equations for conservation of mass, momentum - with an appropriate turbulence model - and energy are used. In order to better correspond with the real flow in a microbubble generator, the CFD model was devised for three-dimensional, unsteady, turbulent flow with constant properties.

Continuity equation

$$\frac{\partial \rho}{\partial t} + \frac{\partial (\rho u_i)}{\partial x_i} = S_m \tag{1}$$

Momentum equations

$$\frac{\partial (\rho u_i)}{\partial t} + \frac{\partial \left(\rho u_i u_j\right)}{\partial x_j} = -\frac{\partial p}{\partial x_i} + \frac{\partial}{\partial x_j}\left[\mu\left(\frac{\partial u_i}{\partial x_j} + \frac{\partial u_j}{\partial x_i}\right)\right] + \frac{\partial \left(-\rho \overline{u_i' u_j'}\right)}{\partial x_j} + \rho g + F \tag{2}$$

Energy equation

$$\frac{\partial(\rho E)}{\partial t}+\frac{\partial(u_i \rho E)}{\partial x_j}=\frac{\partial}{\partial x_j}\left[\left(k_f+\frac{c_p \mu_t}{Pr_t}\right)\frac{\partial T_i}{\partial x_j}\right]+S_h \quad (3)$$

Reynolds stresses are modelled using the Boussinesq approximation: [25]

$$\frac{\partial\left(-\rho\overline{u_i' u_j'}\right)}{\partial x_j}=\mu_t\left(\frac{\partial u_i}{\partial x_j}+\frac{\partial u_j}{\partial x_i}\right)-\frac{2}{3}\rho k \delta_{ij} \quad (4)$$

Turbulent motion of the continuous phase of water are described through the Standard *k*-ε model in Equations (5) and (6), where eddy viscosity adds to the fluid viscosity, directly proportional to the square of the turbulence kinetic energy [25]:

$$\mu_{eff}=\mu+\mu_t \quad (5)$$

$$\mu_t=C_\mu \rho \frac{k^2}{\varepsilon} \quad (6)$$

Transport of the turbulent kinetic energy *k* and its respective dissipation rate ε are modelled in the following scalar Equations (7) and (8), to close the Governing Navier-Stokes equations [25]:

$$\frac{\partial(\rho k)}{\partial t}+\frac{\partial(\rho k u_i)}{\partial x_i}=\frac{\partial}{\partial x_j}\left[\left(\mu+\frac{\mu_t}{\sigma_k}\right)\frac{\partial k}{\partial x_j}\right]+G_k+G_b-\rho\varepsilon-Y_M+S_k \quad (7)$$

$$\frac{\partial(\rho\varepsilon)}{\partial t}+\frac{\partial(\rho\varepsilon u_i)}{\partial x_i}=\frac{\partial}{\partial x_j}\left[\left(\mu+\frac{\mu_t}{\sigma_\varepsilon}\right)\frac{\partial \varepsilon}{\partial x_j}\right]+C_{1\varepsilon}\frac{\varepsilon}{k}(G_k+C_{3\varepsilon}G_b)-C_{2\varepsilon}\rho\frac{\varepsilon^2}{k}+S_\varepsilon \quad (8)$$

The Standard *k*-ε model is often used in different industrial applications and is based on the transport of the turbulent kinetic energy and its rate of

dissipation as explained above in Equations (7) and (8). Its capability to well reproduce turbulence in both external and internal flows at low computational expense, makes it attractive for a variety of flows. The Standard *k*-ε model is computationally sustainable, due to the use of empirical wall functions to model the near-wall region, especially the viscous sub-layer – rather than achieving a fully-resolved flow down to the wall.

In the present calculation, we have initially selected the Standard *k*-ε model mainly for two reasons: a) its economy in terms of computational resource and mesh requirement, and b) the fact that we are simulating two-phase flow with very low volumetric quality, hence, comparable with single-phase flows. In order to reduce the error due to near-wall empirical functions, we have selected the Enhanced Near-wall Treatment option, where a smoothing blending function is used in FLUENT to combine the viscosity-dominant near-wall region with the fully-turbulent region, in the so-called two-layer approach [25]. The demarcation boundary between the two regions is represented by the turbulent Reynolds number, shown in Equation (9) below [25]:

$$Re_y = \frac{\rho y \sqrt{k}}{\mu} \tag{9}$$

Therefore, in the viscous-dominant region ($Re_y < 200$) the turbulent dissipation of kinetic energy ε is computed through Equation ((10), rather than its conventional transport Equation (8), being l_ε the turbulent scale defined by Chen and Patel [29]:

$$\varepsilon = \frac{k^{3/2}}{l_\varepsilon} \tag{10}$$

Note that the above turbulence model is a closure for the continuous phase of water only, whereas dispersion of particles due to turbulence is modelled separately, through the stochastic tracking model in FLUENT [25]. Trajectory of bubbles is definitely affected by local turbulent velocity fluctuations and computed through implicit-trapezoidal order discretisation scheme.

Furthermore, the Lagrangian Discrete Phase Model (DPM) is used to determine air bubbles in the form of dispersed particles in water. DPM allows a mutual interaction in the form of interphase momentum exchange between particles and surrounding fluid. In this way, particle trajectory is

dependent on local turbulence of the continuous phase, while turbulence can be generated or dissipated (through disruption of the momentum transfer mechanism [30]), due to the presence of discrete bubbles.

3.2 Bubble equation

Prediction of the particle trajectory is based on integrating the force balance on the particle, which is based on Lagrangian formulation. [26, 27] The balance of inertia, drag and gravitational forces acts on the particle in the longitudinal direction as: [25]

$$\frac{du_p}{dt} = F_D\left(u - u_p\right) + \frac{g_x\left(\rho_p - \rho\right)}{\rho_p} \tag{11}$$

$$F_D = \frac{18\mu}{\rho_p d_p^2}\frac{C_D Re}{24} \tag{12}$$

Where the term $F_D\left(u - u_p\right)$ is the drag force per unit particle mass and F_D the drag force encountered by the particle. Furthermore, u is the air velocity, C_D the drag coefficient, u_p is the particle velocity, μ is the air viscosity, ρ is the air density, ρ_p the particle density and d_p is the particle diameter. Re is the relative Reynolds number which is defined in Equation (13).

$$Re = \frac{\rho d_p \left|u_p - u\right|}{\mu} \tag{13}$$

The Rosin-Rammler method is used to define the bubble distribution at the injection surface of the microbubble generator (Figure 1b). The model assumes that the particle diameter d_p varies exponentially with the mass fraction of bubbles with diameter larger than d_p, namely Y_d, as shown in Equation (14) where *n* is the size distribution parameter and $\bar{d}$ is a size constant [25]:

$$Y_d = e^{-(d/\bar{d})^n} \tag{14}$$

In order to ensure consistency with the experimental setup from Sadatomi et al. [8,19] - where punched-hole surfaces with hole diameters ranging from 0.3 to 0.7mm were used for suction of air - we have setup an injection bubble distribution with mean diameter equal to 0.6mm. In this way, we can also

assess whether the design of microbubble generator is able to break injected clouds of bubbles into finer distributions at the nozzle outlet surface.

3.3 Numerical procedure

The numerical setup in ANSYS Fluent V18.1 consists of coupling the discrete phase model (DPM) with the Rosin-Rammler method to produce a cloud of microbubbles at the MBG outlet section.

The discrete phase model utilizes a lagrangian approach to derive the equations for the underlying physics which are solved transiently. Transient numerical procedures in the discrete phase model can be applied to resolve steady flow simulations as well as transient flows. Therefore, steady state trajectory simulations can be performed even when selecting a transient solver. Vice versa, unsteady particle tracking can be selected when solving the steady continuous phase equations.

In the present study, as mentioned in Section 3 the continuous phase of water is treated as unsteady flow together with the discrete phase. The above coupling not only is helpful to improve numerical stability for very large particle source terms, but it can reproduce the unsteady flow mechanisms taking place during the injection of discrete bubbles. Discrete particles are transported and interact with the fluid and are tracked with the same time step settings. In this way, the particle trajectory is calculated step by step, while advancing to a new position. Considerations relative to the DPM injection velocity and particle motion equations have led us to infer that a maximum time step equal to 10ms is acceptable to capture the particle trajectory and satisfy the CFL criterion for explicit solver formulation (maximum Courant number, $C_{MAX} = 1$).

Furthermore, since turbulence can affect the dispersion of particles, the stochastic tracking approach has been enabled for prediction of the particles turbulent dispersion, by making use of the instantaneous flow velocity:

$$u(t) = \overline{u(t)} + u'(t) \tag{15}$$

In order to achieve a reasonable prediction of the particles dispersion, DPM trajectories are integrated through the integral time scale T, defined as the time interval where the infinitesimal particle path ds is in turbulent regime:

(16)

$$T = \int_0^\infty \frac{u_p'(t)}{\overline{u_p'^2}} ds$$

In the assumption that there is no relative velocity between the particle and surrounding fluid, the integral time scale T becomes equal to the fluid Lagrangian integral time, which is proportional to the ratio between the turbulent kinetic energy, k, and the turbulent dissipation rate, ε. At this stage, the Realizable k - ε turbulence model is valuable, since the assumption of isotropic flow is preferable to reduce the computational cost and to simplify models, while improving accuracy on separated flows and swirling motions.

Finally, unstructured tetrahedral grid is produced in ANSYS Meshing V18.1. An inflation layer, composed of 11 sublayers with growth rate equal to 1.2 and first layer thickness of 5.0e^{-05}m is set to accurately resolve the viscous sublayer (Figure 3) and corresponding to a desired value of the non-dimensional distance of the centroid of wall attached cells, namely $y^+ = y\rho u^*/\mu = 1$ (being u^* the friction velocity and μ the dynamic viscosity of water at ambient temperature). Although the $y^+ = 1$ condition is not strictly required with the Standard $k - \varepsilon$ model (due to the use of wall functions), we believe that a fine mesh near the wall can help to improve the near-wall solution.

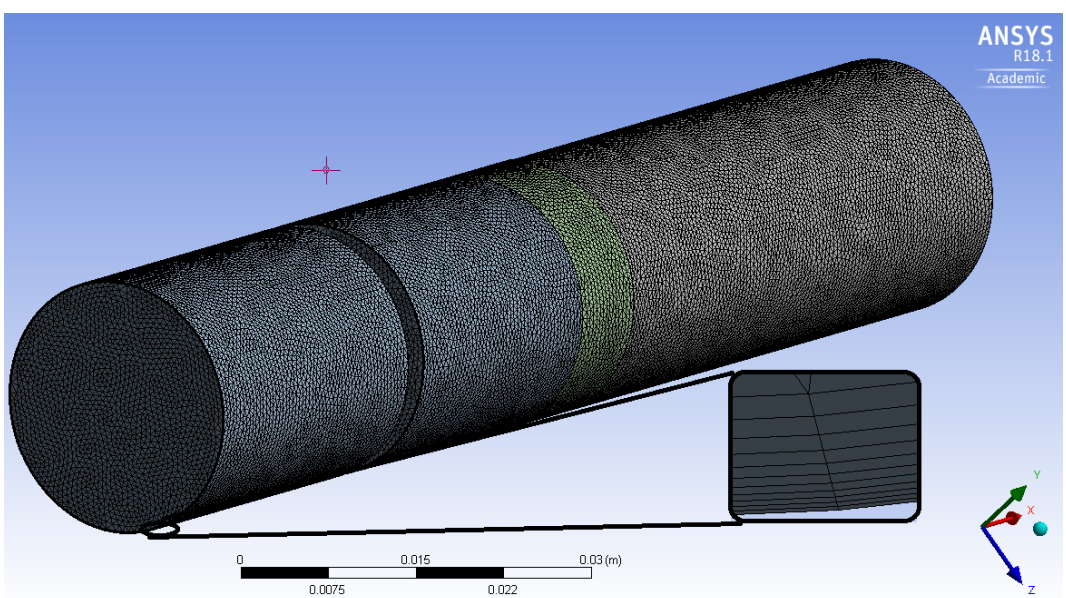

Figure 3. Grid layout for the orifice microbubble generator.

To further convalidate our approach, a mesh-independence study has been

carried out at each flow condition and geometry, by ensuring that the flow rate unbalance between inlets and outlet is, at most, equal to 1%. Furthermore, simulation results have been consolidated by assigning a convergence criterion for all residuals equal to $1.0e^{-05}$, in order to establish a high-level solution accuracy. Convergence of the net mass flow rate through the entire volume is monitored to further ensure that the overall calculation has properly converged.

4. Results and discussion

4.1 Orifice-type tube

The orifice microbubble generator has been discussed by Sadatomi et al. [19], inferring that orifice induces bubble breakup, which produces microbubbles of mean diameter equal to 95.2 μm (Figure 4).

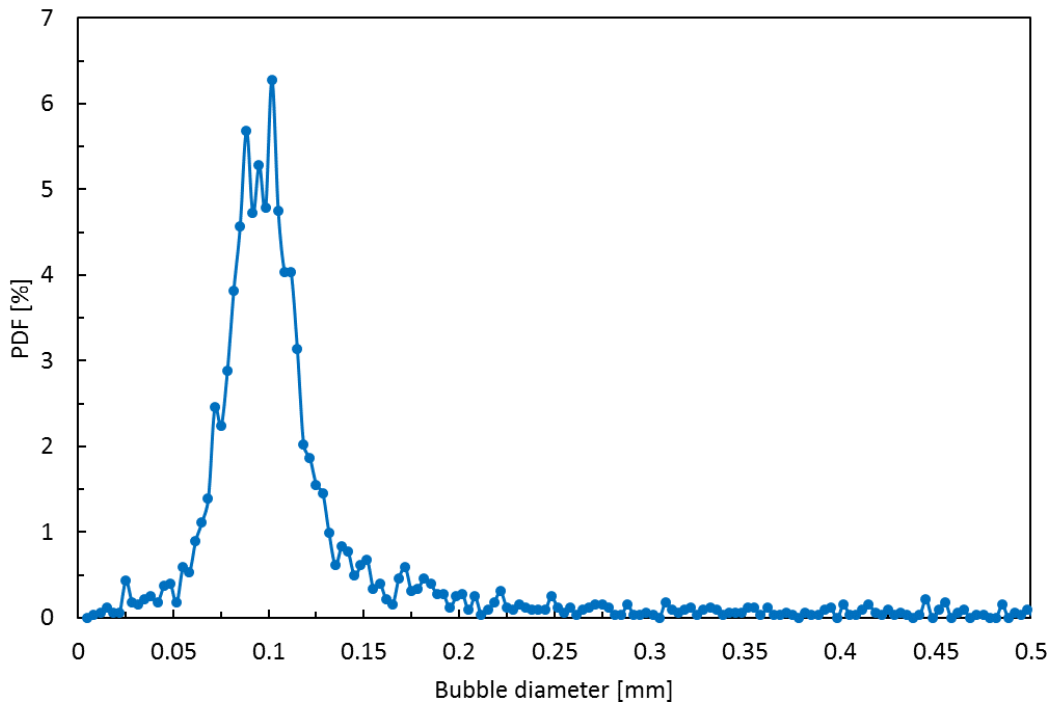

Figure 4. Histograms of particle diameter near the pressure outlet face from the CFD simulation. $\alpha = 5.71\%$.

A direct comparison with Sadatomi's results is presented in Figure 5, where the Sauter mean diameter from numerical simulation – defined as $d_{BS} = 6 \times \sum n_i \pi d_{Bi}^3 / \sum n_i \pi d_{Bi}^2$, being d_{Bi} the diameter of a single bubble – is plotted versus the mean flow velocity at the orifice center - namely $V_{L2} = 4Q_L/\pi d_0^2$, where Q_L is the water flow rate and d_O the orifice diameter. The bubble

diameter at the nozzle outlet from Sadatomi's work ranges from 0.6 to 2.65 mm.

By contrast, results from present simulation show Sauter diameters which are 200 - 500μm, having the largest variations at high volumetric qualities. This discrepancy might be explained with the fact that - in Sadatomi's experiment – air is introduced in the tube by suction, as a result of the recovery pressure drop. By contrast, CFD simulation assumes air injection through the porous wall. Furthermore, the presence of the orifice in the tube induces severe pressure variation, flow separation, and local recirculation, resulting in different flow structures - varying with boundary conditions and geometry – which cannot be easily resolved. All the above considerations may affect the mutual interaction between continuous and dispersed phases, which results in a different microbubble distribution at the tube outlet surface, compared to experiments.

For the reasons mentioned above, we have tested our CFD model on the Venturi microbubble generator, which – as described in Section 4 – has better reproduced the experimental results from the literature. Presumably, the design of a Venturi microbubble generator, characterized by a convergent-divergent tube, produce a more gradual variation in the flow variables compared to orifice, hence, developed flow structures are easier to be resolved. Therefore, we have shifted our investigation on microbubble performance towards Venturi tubes.

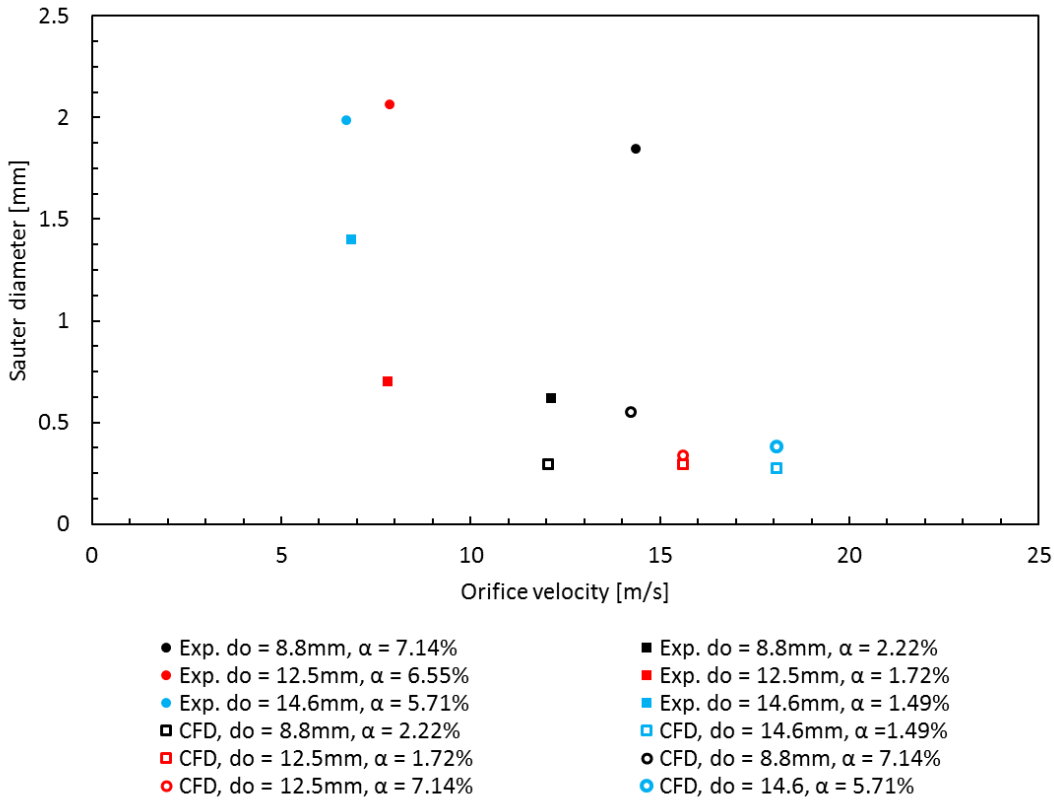

Figure 5. Sauter mean diameter versus mixture velocity at the orifice, for different orifice diameters d_0. Experimental data from Sadatomi et al. [19].

4.2 Venturi microbubble generator

Venturi microbubble generators are of interest as they do not require any moving components. Therefore, there is no additional power input required, apart from the apparatus pressurizing the air-water mixture into the tube. The above condition means a more efficient energy management for a shrimp nursery farms. Moreover, bubble breakup is facilitated here by pressure recovery, downstream of the throat section, which results in a further shift of the mean diameter towards smaller values, compared to orifice-type generators. Bubble breakup occurs right after the throat section, where turbulent pressure fluctuations achieve their maximum intensity.

Results from CFD simulations in Figure 6 show that the region near the nozzle exit, namely $x = 0.06 - 0.075$ m (being the inlet test section located at $x = 0.0$ m), is where microbubbles accumulate in largest amounts and where it is likely to have the finest and most uniform clouds. Size of

microbubbles in this region is described by their distributions in Figure **7**, where we have compared our numerical results with the experimental data from Kawashima et al. [22] Results are in agreement on mean diameters being in the range 90 - 150 µm.

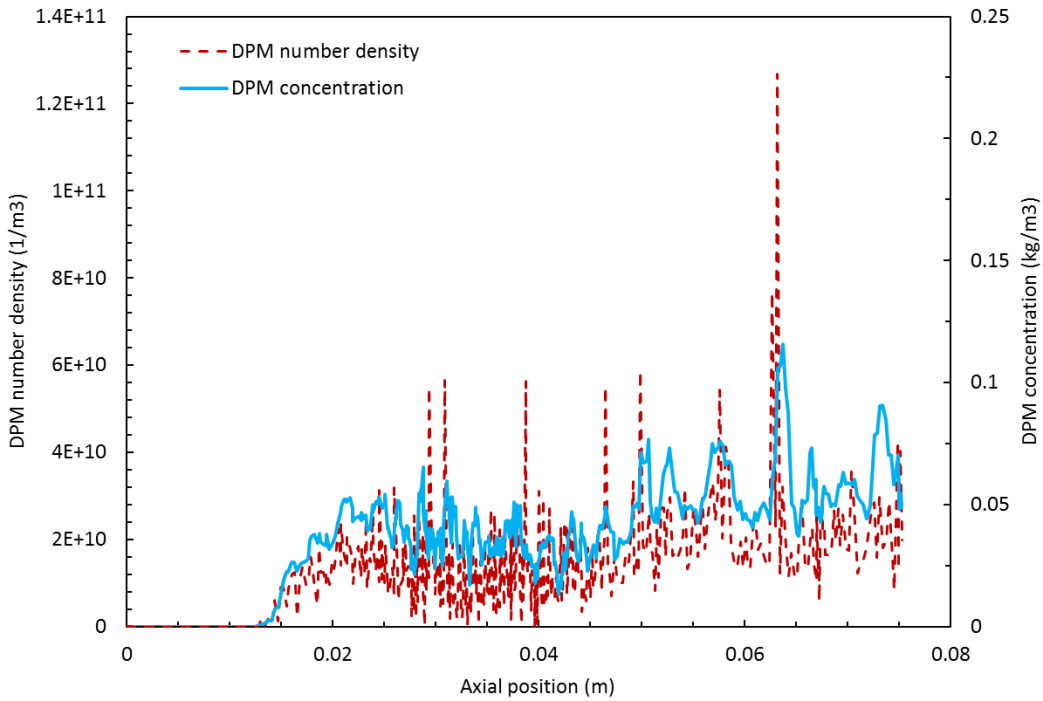

Figure 6. DPM number density (1/m^3) and concentration (kg/m^3) along the center line of the baseline Venturi microbubble generator.

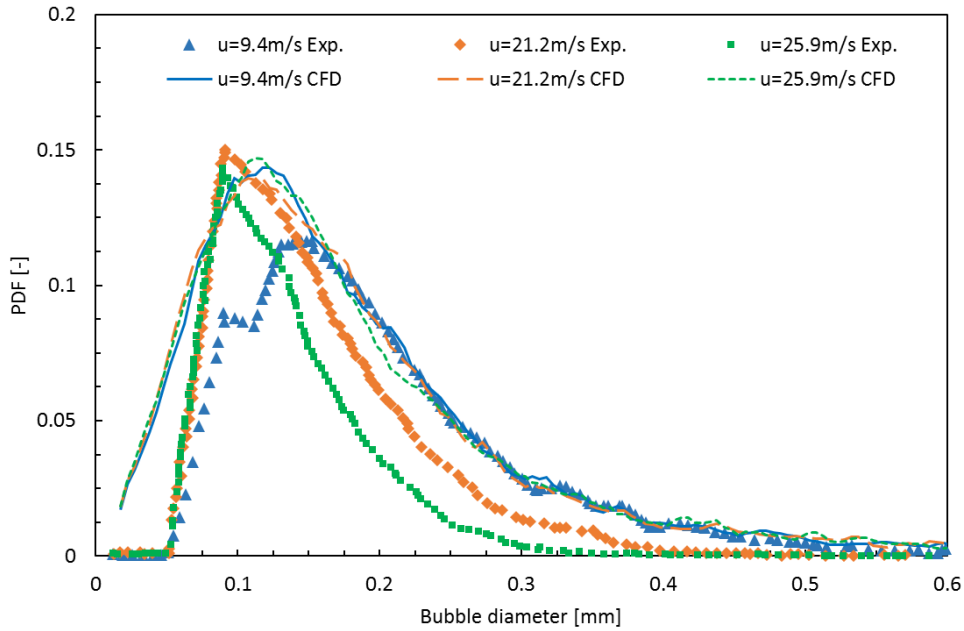

(a)

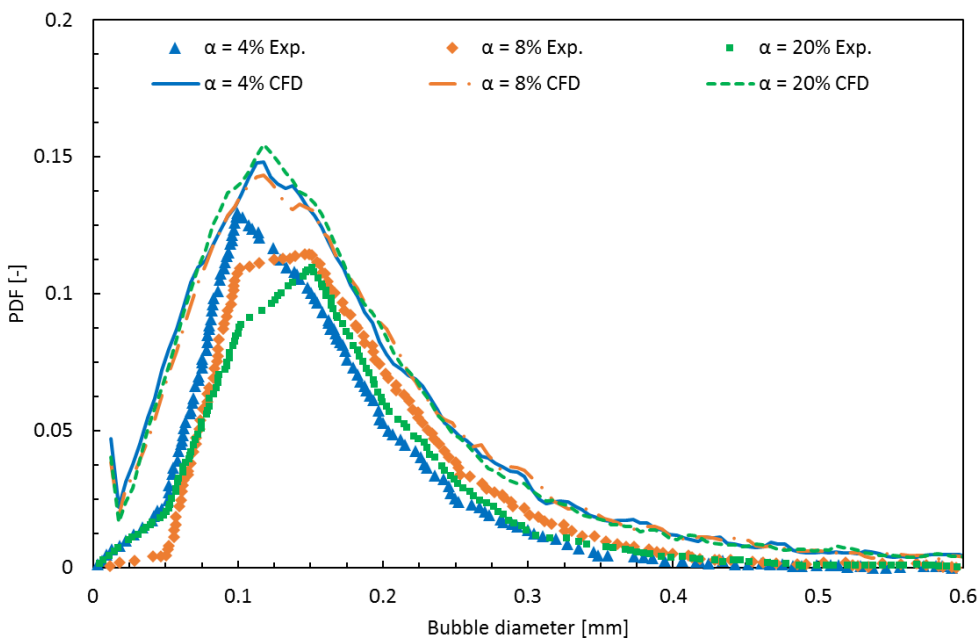

(b)

Figure 7. Comparison of CFD and experimental data from Kawashima et al. [22]: a) fixed volumetric quality ($\alpha = 4\%$), and b) fixed throat velocity ($u_{th} = u_{th} = 16$ m/s).

4.3 Modified Venturi-type tube

Results in previous sections (Figure 5 and Figure **7**) have proved that Venturi microbubble generators are more effective in straining and breaking bubbles, compared to orifice-type tubes. With this idea in mind, we have modified the baseline Venturi generator to achieve any possible decrements in the mean diameter below 50 μm, by removing an axial helicoid volume of material from the tube – here named as *helicoid* (Figure 8a) – at three different pitch angles, namely $\beta = 10^o, 20^o, 30^o$. In this way, we intend to produce a two-phase flow field characterized by strong swirling motions, which can produce a higher shear stress and induce a finer and more uniform distribution of microbubbles at the tube outlet.

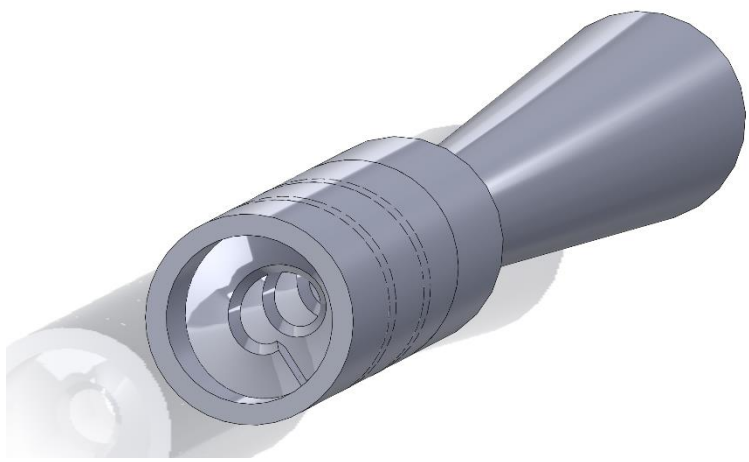

(a)

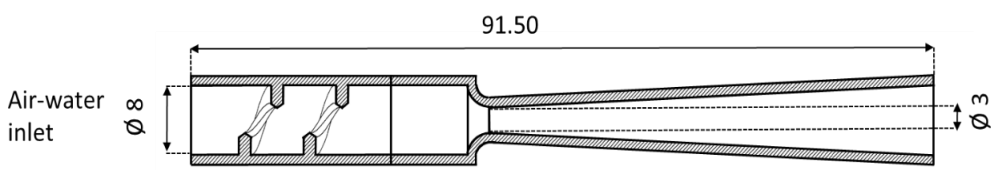

(b)

Figure 8. Modified Venturi microbubble generator. Pitch angle $\beta = 20^o$. Dimensions in mm. a) 3D design and b) longitudinal section.

Effects of the modified configuration captured from the CFD simulation are resumed below:

- The presence of the helicoid induces an axial flow acceleration so that the stream-wise velocity, culminating at the throat section,

dominates over the circular tangential component. Swirling motion persists downstream of the throat section so that bubbles are subject to a dual effect with turbulent pressure fluctuations.

- The particular shape of the modified microbubble generator suggests the formation of trains of turbulent eddies, detaching from the helicoid upper edge. The shear layer produced is believed to be the interface region between swirling flow and the main longitudinal component of motion - which includes dispersed air bubbles, being these injected at the inlet center line of the tube.
- Vortices produced from the helicoid configuration tend to accumulate at the throat and to facilitate bubble breakup in the pressure recovery zone. In fact, CFD simulations show that bubbles with diameter from 100 µm to 175 µm are uniformly distributed at the nozzle exit section (Figure 9).

Trends above have been confirmed by other researchers [21, 22, 28] and may be attributed to a combination of coalescence and breakup of bubbles at the throat section.

The same inlet conditions as in Table 2 have been selected for the modified version of the Venturi microbubble generator. Histograms of bubble diameters produced from CFD are compared with experimental measurements of the baseline Venturi generator previously investigated by Kawashima et al. [22] A good agreement in terms of mean diameter of the bubble distribution is observed in Figure 9 and Figure 10. More accurate results are shown in Figure 11 where the mean diameter of bubble distributions is reported at different throat velocities.

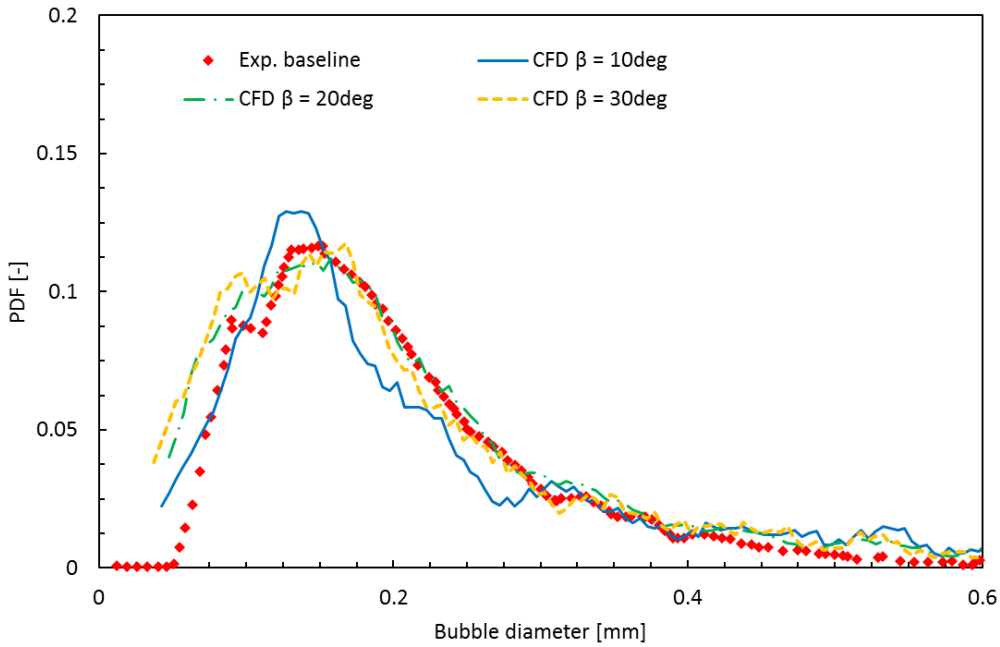

Figure 9. Distributions of bubble diameters at fixed air fraction ($\alpha = 4\,\%$) and throat velocity ($u_{th} = 9.4$ m/s), for different helicoid pitch angles. Comparison with baseline experimental results from Kawashima et al. [22].

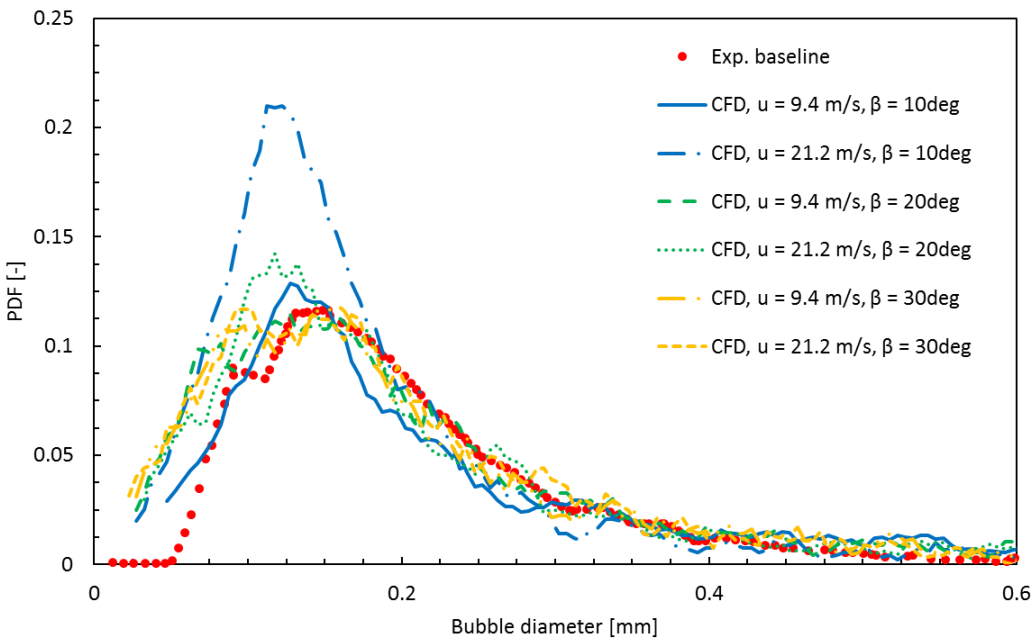

Figure 10. Bubble distribution at fixed air fraction ($\alpha = 4\,\%$), at different helicoid pitch angles and throat velocities. Baseline data from Kawashima et al. [22].

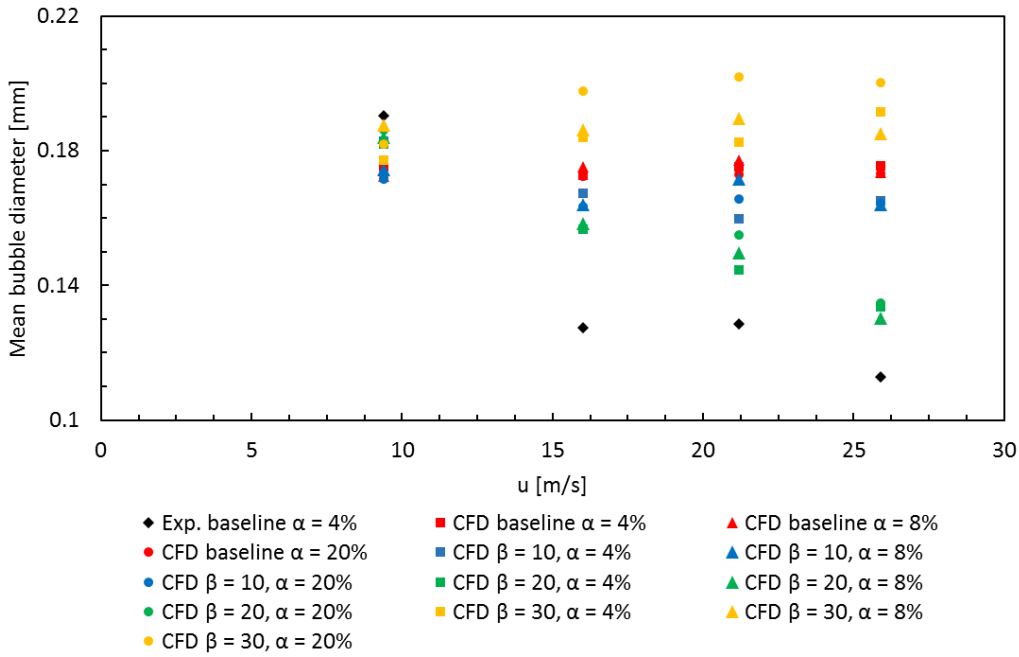

Figure 11. Mean bubble diameters from experiments (baseline Venturi) [22] and CFD simulations (modified Venturi) at different helicoid angles β (degrees) and throat velocities.

Results from Figure 11 are summarized in the following points:

- CFD results, especially the modified cases $\beta = 10^o, 20^o$ reproduce the trend of experimental data, in the sense that smaller microbubbles correspond to higher inlet velocities of the air-water mixture.
- For low velocity at the throat section ($u_{th} = 9.4$ m/s) all the three modified cases ($\beta = 10^o, 20^o, 30^o$) produce smaller mean diameters than the baseline case, with a maximum variation equal to 30 μm between the experimental measurements from Kawashima et al. [22] and the case $\beta = 10^o$, $\alpha = 20\%$. This result is of interest for power consumption considerations in further developments.
- For high velocities ($u_{th} \geq 9.4$m/s), the baseline Venturi tube from Kawashima et al. [22] produces smaller bubbles, compared to all modified configurations. The modified case $\beta = 30^o$, $\alpha = 20\ \%$ has the largest discrepancy from experimental measurements, with an increase in mean diameter between 70 μm and 80 μm, at $u_{th} = 25.9$

m/s. This result suggests that the modified configuration is not efficient at high flow rates.

- The pitch angle $\beta = 20^o$ is the best geometrical compromise, as it satisfactorily reproduces the trend of experimental data, especially at $u_{th} = 25.9$ m/s and $\alpha = 8\,\%$, where bubble distributions with mean diameter of 130 μm are produced.

To summarize, numerical simulations suggest an optimal geometry with pitch angle $\beta = 20^o$ and air fraction $\alpha = 20\,\%$ in good agreement with experiments. [22, 19] Therefore, the above design would require a further experimental validation to establish the CFD setup proposed in this work.

5. Conclusions

Two different methods of microbubble generation have been investigated through CFD methods. Results were compared with experimental data for orifice (Sadatomi et al. [19]) and Venturi baseline (Kawashima et al. [22]) microbubble generators. Results show discrepancy between numerical simulations and Sadatomi's results, which is attributed to flow recirculation downstream the orifice, which cannot be accurately modelled in Fluent.

By contrast, present calculations are in agreement with Kawashima's measurements. Therefore, a reliable CFD setup, making use of the Discrete Phase Model (DPM) coupled with Rosin-Rammler distribution method, has been established with satisfactory accuracy.

Since the CFD model is well reproducing experimental data for Venturi microbubble generators, we have proposed an innovative geometry where a helicoid extrusion of material is applied to the tube. Helicoid pitch angles $\beta = 10^o, 20^o, 30^o$ have been used, attempting to reduce the mean diameter of microbubble distributions below 50 μm.

Optimal flow condition (at high inlet velocity) and geometry have been identified in $u_{th} = 25.9$ m/s, $\alpha = 8\,\%$, and $\beta = 20^o$, where microbubbles as small as 130 μm were reproduced. Additionally, at low inlet speed all modified configurations perform better than the experimental Venturi baseline generator. This result is encouraging us to further experimental investigation to validate the current numerical results.

The above developments are beneficial for shrimp nursery facilities, where the size of micro-bubbles is crucial to control the level of dissolved-oxygen in water. Results presented in this work can actively contribute to increase the productivity of shrimp farms, while smaller amounts of clean water are used.

ACKNOWLEDGMENTS

This work has been funded by EPSRC under the grant agreement no. EP/P018211/1, in collaboration between Teesside University, UK, and University of Malaya, Malaysia.

NOMENCLATURE

C_μ	Constant to define the turbulent dynamic viscosity [-]
d_B	Bubble diameter [mm]
d_{BS}	Bubble Sauter diameter [mm]
d_E	Diameter of a turbulent eddy [mm]
d_H	Diameter of punched holes across porous wall [mm]
d_{IO}	Inlet diameter for water injection in the orifice generator [mm]
d_o	Orifice diameter in the orifice-type bubble generator [mm]
d_N	Needle diameter for air injection in the Venturi-type generator [mm]
d_p	Diameter of the dispersed particle [mm]
DAF	Dissolved air flotation
DO	Dissolved oxygen
DPM	Discrete phase model
MGB	Micro-bubble generator
e_n	Non-dimensional coefficient of elastic restitution of energy [-]
f_n	Bubble natural frequency [Hz]
h_H	Height of the cylindrical porous wall [mm]
k	Turbulent kinetic energy [m^2/s^2]
Q_g	Mass flow rate of air [kg/s]
Q_l	Water flow rate [l/min]
u	Stream-wise velocity of water [m/s]
u_{th}	Stream-wise velocity at the throat section of Venturi tube [m/s]
We	Weber number [-]
Y_d	Mass fraction of bubbles with diameter larger than d_p [-]

Greek letters

α	Air volumetric quality in water [-]
β	Helicoid pitch angle for the modified Venturi generator [deg]
ε	Turbulence dissipation rate [m^2/s^3]
μ	Dynamic viscosity of fluid [Ns/m^2]
μ_t	Turbulent viscosity [Ns/m^2]

ρ_p Density of the dispersed particle/bubble [kg/m^3]

ρ Density of water [kg/m^3]

σ Bubble surface tension [N/m]

REFERENCES

[1] Ohnari H, Fisheries experiments of cultivated shells using micro-bubbles technique, Journal of the Heat Transfer Society of Japan - 40, 2001, 2-7.

[2] Gillot S, Capela-Marsal S, Roustan M, Héduit A, Predicting oxygen transfer of fine bubble diffused aeration systems - model issued from dimensional analysis, Water Research , 39, 2005, 1379-1387.

[3] Fayolle Y, Cockx A, Gillot S, Roustan M, Héduit A, Oxygen transfer prediction in aeration tanks using CFD - 62, Chemical Engineering Science, 2007, 7163-7171.

[4] Marui T, An introduction to micro/nano bubbles and their applications., The 14th World Multi-Conference on Systemics, Cybernetics and Informatics, vol. 1, 2010.

[5] Argawal A, Jern W, Liu Y, Principle and applications of microbubble and nanobubble technology for water treatment, Chemosphere, 84, 2011, 1175-1180.

[6] Endo A, Srithongouthai S, Nashiki H, Teshiba I, Iwasaki T, Hama D, Tsutsumi H, DO-increasing effects of a microscopic bubble generating system in a fish farm, Marine Pollution Bulletin 57, 2008, 78-85.

[7] Takahashi M, “Constriction and collapse of micro-bubbles, Lecture Series of the Japanese society for Multiphase Flow, 28, 2003, 15-19.

[8] Sadatomi M, Kawahara A, Kano K, Ohtomo A, Performance of a new micro-bubble generator with a spherical body in a flowing water tube., Experimental Thermal and Fluid Science, 29, 2005, 615-623.

[9] Fujikawa S, Zhang R, Hayama S, Peng G, The control of micro-bubble generation by arotational porous plate, International journal of Multiphase Flow, 29, 2003, 1221-1236.

[10] Amaral Filho J, Azevedo A, Etchepare R, Rubio J, Removal of sulfate ions by dissolved air flotation (DAF) following precipitation and flocculation, Int. Jou. of Mineral Processing, 149, 2016, 1-8.

[11] Rubio J, Carissimi E, Rosa J, Flotation in water and wastewater treatment and reuse: recent trends in Brazil, International Journal of Environment and Pollution, 30, 2007, 197-212.

[12] Edzwald J, Haarhoff j, Dissolved air flotation for water clarification, McGraw-Hill, 2012.

[13] Hague J, Experimental and modeling study of two-phase flow (air-water) in dissolved air flotation (DAF) tanks, EngD thesis - University of Surrey, 1, 2003.

[14] Creamer k, Chen Y, Williams C, Cheng J, Stable thermophilic anaerobic digestion of dissolved air flotation (DAF) sludge by co-digestion with swine manure, Biores. Tech., 101, 2010, 3020-3024.

[15] Yoo S, Hsieh J, Advanced water recycling through electrochemical treatment of effluent from dissolved air flotation unit of food processing industry, Water Science Technology, 61, 2010, 181-190.

[16] Al-Thyabat S, Al-Zoubi H, Purification of phosphate waste-water: separation of phosphate from Eshydia Mine by column-DAF flotation process, Int. Jou. of Mineral Processing, 110-111, 2012, 18-24.

[17] Rodrigues R, Rubio J, DAF-dissolved air flotation: potential applications in the mining and mineral processing industry, International Journal of Mineral Processing, 82, 2007, 1-13.

[18] Moursy A, Abo El-Ela S, Treatment of oil refinery waste using dissolved air flotation process, Environ. Int., 7, 1982, 267-270.

[19] Sadatomi M, Kawahara A, Matsuura H, Shikatani S, Micro-bubble generation rate and bubble dissolution rate into water by a simple multi-fluid mixer with orifice and porous tube., Exp. Thermal and Fluid Science, 41, 2012, 23-30.

[20] Tabei K, Haruyama S, Yamaguchi S, Study of micro bubble generation by a swirl jet, Transactions of the Japanese Society for Mechanical Engineering, 71, 703B, 2007, 848-853.

[21] Kawamura T, Fujiwara A, Takahashi T, Kato H, Matsumoto Y, Kodama Y, The effects of the bubble size on the bubble dispersion and skin friction reduction, Proceedings of the fifth symposium on smart control of turbulence, Tokyo, 2004.

[22] Kawashima H, Fujiwara A, Saitoh Y, Hishida K, Kodama Y, Experimental study of frictional drag reduction by microbubbles: laser measurement and bubble generator, Proceedings of the fifth symposium on smart control of turbulence, Tokyo, 2004.

[23] Ishikawa M, Irabu K, Teruya I, Nitta M, PIV measurement of a contraction flow using micro-bubble tracer, The sixth symposium on measurement techniques for multi-phase flows, 2009.

[24] Gordiychuk A, Svanera M, Benini B, Poesio p, Size distribution and Sauter mean diameter of micro bubbles for a Venturi type bubble generator, Experimental Thermal and Fluid Science, 70, 2016, 51-60.

[25] ANSYS Fluent, [Online]. Available at: http://www.ansys.com/Industries/Academic/Tools/Citations.

[26] Jin-song Z, Zhonh-yang l, Xiang G, Ming-Jiang N, Ke-Fa C, Effect of particle loading ratio on heat transfer enhancement in a gas-solid suspension cross flow, Hangzhou, China, 2002.

[27] Stakic M, Zivkovic G, Sijercic M, International Journal of Heat and Mass Transfer, 54, 2011, 2262.

[28] Yin J, Li J, Li H, Liu W, Wang D, Experimental study on the bubble generation characteristics for a Venturi type bubble generator, International Journal of Heat and Mass Transfer, 91, 2015, 218-224.

[29] Chen, HC and Patel, VC, Near-wall turbulence models for complex flows including separation. AIAA Journal, 26(6), 641-648, 1988.

[30] Maxei, MR, Chang, EJ and Wang, LP, Interactions of Particles and Microbubbles with Turbulence, Experimental Thermal and Fluid Science, 12, 417-425, 1996.